SUPPLEMENTARY INFORMATION

Day-Night imaging without Infrared Cutfilter Removal based on metal-gradient perovskite single crystal photodetector

Yao Ma[1†], Leting Shan[2†], Yiran Ying[3†], Liang Shen[1†], Yufeng Fu[2], Linfeng Fei[2], Yusheng Lei[4], Nailin Yue[5], Wei Zhang[5], Hong Zhang[4], Haitao Huang[3], Kai Yao[2]*, and Junhao Chu[4]

Supplementary Methods

Other characterization: Thermogravimetric analysis (TGA) measurements were carried out using a Mettler Toledo SDTA 851e. NMR measurements were performed for samples dissolved in deuterated DMSO (DMSO-d6) in liquid-state ^{1}H-NMR 600 MHz instruments. X-ray crystallography characterization of the crystals was conducted on a Bruker AXS (Mo Kα) at 173 K. AES mapping was performed on a PHI 710 Scanning Auger Nanoprobe instrument with a 10 keV/10 nA primary electron beam and 128 × 128 pixel resolution. The current-voltage characteristics and the SCLC were measured using a Keysight B2901A sourcemeter. TPC measurements were performed using a 532 nm nanosecond pulsed laser, Stanford Instruments SR570 low-noise current amplifier, and Keysight DSOX6004A oscilloscope. The noise current spectra were analyzed by a ProPlus 9812D wafer-level 1/f noise characterization system and a Keithley 4200 semiconductor parameter analyzer. Response speed and frequency response characteristics are conducted using white LED, infrared LED, current amplifier, and oscilloscope. For the characterization of long-term stability, the signal response of the detector to a white LED (10 mW cm^{-2}) was collected under ambient conditions with around 40% humidity.

ICP-OES: Before ICP-OES measurements, we first prepared a single stock solution of 50 ppm Pb and 5 ppm Sn by diluting the Pb (1000 ppm) and Sn (1000 ppm) ICP standard solutions. Then, the calibration standards ranging from 125 ppb Pb to 50 ppm Pb and 12.5 ppb Sn to 5 ppm Sn were obtained. Next, we dissolved our Pb−Sn alloyed perovskite crystals in concentrated nitric acid and diluted them to parts per billion (ppm) concentrations. Finally, we measured standard and sample solutions in the mode of continuous run.

Computational details: First-principles calculations were performed in the framework of density functional theory (DFT) by the Vienna *ab initio* simulation package (VASP)[1,2]. The Perdew-Burke-Ernzerhof (PBE) flavor of generalized gradient approximation was used in the calculations[3], and the DFT-D3 scheme was applied for the van der Waals corrections[4]. The plane-wave cut-off energy was set as 400 eV. The energy and force convergence criteria were set as 1×10^{-5} eV and 0.02 eV/Å, respectively. A vacuum layer of more than 15 Å was applied to avoid spurious interactions between adjacent cells. The supercell structure of pure-Pb perovskite ($Cs_2FA_{15}GA_1Pb_{18}I_{51}Br_3$) was constructed by replacing three FA ions with two Cs and one GA, and three I ions with Br randomly on the 3×3×2 supercell of $FAPbI_3$ ($FA_{18}Pb_{18}I_{54}$). We

optimized structures of pure-Pb perovskites by giving the lowest formation energy.

For direct Pb-Sn alloying channel, the energy difference ΔE for Sn replacing Pb was calculated as $\Delta E = E_{(\text{Pb-Sn perovskite})} - E_{(\text{Pb perovskite})} - E_{(\text{Sn})} + E_{(\text{Pb})}$, where $E_{(\text{Pb-Sn perovskite})}$, $E_{(\text{Pb perovskite})}$, $E_{(\text{Sn})}$, and $E_{(\text{Pb})}$ represent DFT-calculated energies for Pb−Sn alloyed perovskite surface with one Sn atom doping, pure Pb perovskite surface, Sn atom, and Pb atom in the most stable bulk form, respectively.

For O_2-incorporated channel, the energy difference ΔE for Sn replacing Pb was calculated as $\Delta H = E_{(\text{Pb-Sn-O2 perovskite})} - E_{(\text{Pb perovskite})} - E_{(\text{Sn})} + E_{(\text{Pb})} - E_{(\text{O2})} + E_{(\text{I})}$, where $E_{(\text{Pb-Sn-O2 perovskite})}$, $E_{(\text{Pb perovskite})}$, $E_{(\text{Sn})}$, $E_{(\text{Pb})}$, $E_{(\text{O2})}$, and $E_{(\text{I})}$ represent DFT-calculated energies for O_2-incorporated Pb−Sn alloyed perovskite surface with one Sn atom doping, pure Pb perovskite surface, Sn atom, Pb atom, O_2 molecule, and I atom in the most stable bulk form, respectively.

For investigating and comparing the ability of vacancy formation of different structures, we defined the difference in vacancy formation energy as (1)[5]:

$$DE^{f}_{vacancy} = (E_{\text{vacancy}} - E_{\text{perfect}})_A - (E_{\text{vacancy}} - E_{\text{perfect}})_B \quad (1)$$

where $DE^{f}_{vacancy}$ are the difference in formation energies between the vacancy formation energy of A and B; E_{vacancy} and E_{perfect} are DFT- calculated energies of the structures with and without vacancy, respectively; A and B represent different structures.

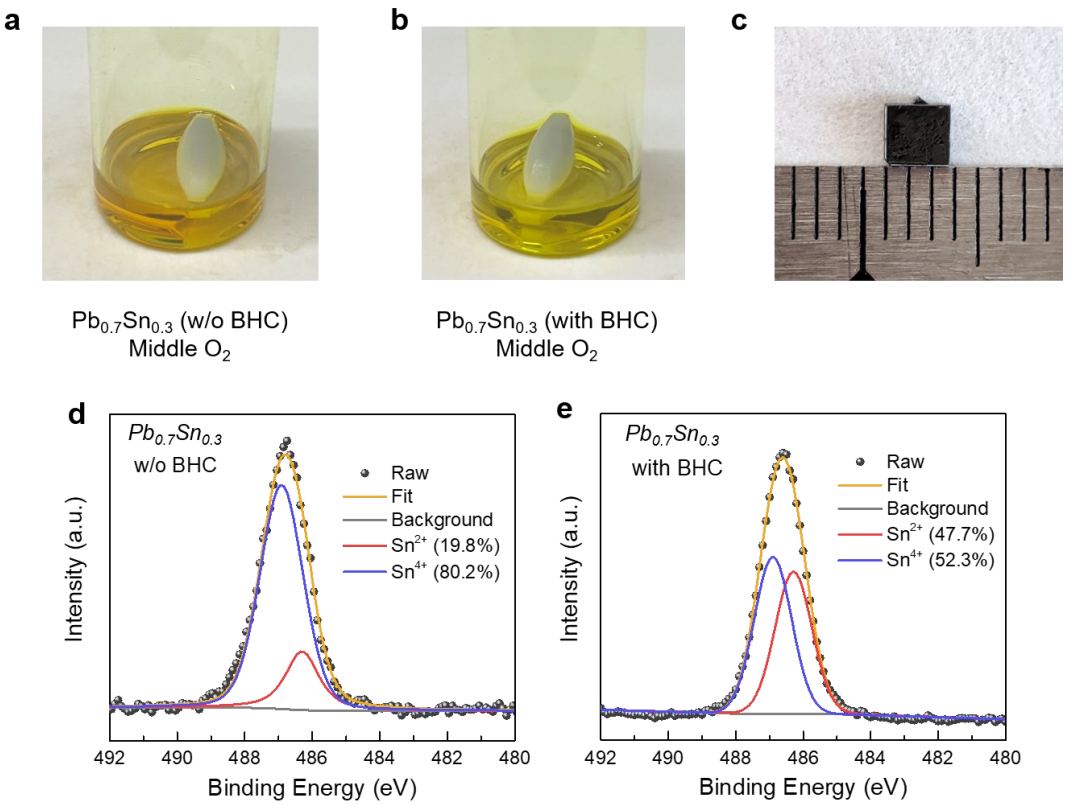

Supplementary Figure 1. The preparation of Pb−Sn alloyed single crystals. a,**b**, Photographs showing the facile reduction by incorporating tiny amounts of benzylhydrazine hydrochloride (BHC). **c**, The Pb−Sn alloyed single crystal prepared without BHC shows a rough and inhomogeneous surface. **d**,**e**, High-resolution XPS spectra of Sn 3*d*5/2 core levels performed on perovskite crystal surfaces prepared without and with BHC antioxidant.

Note: We chose a less-active reductant BHC to restore Sn^{4+} to Sn^{2+} in the raw material during the solution preparation process[6]. Hydrazine compounds are well-explored reducing agents, the addition of tiny amounts of BHC reduce the impurity in starting materials, such as oxidized Sn (Sn^{4+}) impurity. All the XRD patterns (Supplementary Figures 4 and 7) show similar characteristic peaks corresponding to a cubic perovskite structure without impurity, indicating that BHC is not incorporated into the perovskite crystal structure.

Supplementary Table 1. Summary of B-site metal atomic ratios, lattice parameters, and optical bandgap in the single crystals prepared with the feed solution of $Pb_{0.8}Sn_{0.2}$, $Pb_{0.7}Sn_{0.3}$, and $Pb_{0.6}Sn_{0.4}$.

Feed ratio	Oxygen concentration	Sn atomic ratios[a]	Lattice parameters[b]
20% ($Pb_{0.8}Sn_{0.2}$)	10 ppm	1.79 ± 0.12	6.352 ± 0.006
30% ($Pb_{0.7}Sn_{0.3}$)	10 ppm	2.98 ± 0.17	6.321 ± 0.006
40% ($Pb_{0.6}Sn_{0.4}$)	10 ppm	4.39 ± 0.21	6.285 ± 0.006
30% ($Pb_{0.7}Sn_{0.3}$)	1 ppm	2.94 ± 0.17	6.326 ± 0.006
30% ($Pb_{0.7}Sn_{0.3}$)	100 ppm	3.05 ± 0.18	6.319 ± 0.006

Supplementary Table 2. Main composition in the feed solution of $Pb_{0.8}Sn_{0.2}$, $Pb_{0.7}Sn_{0.3}$, and $Pb_{0.6}Sn_{0.4}$ single crystals prepared under the same middle oxygen concentration atmosphere, calculated from the results of XPS and ^{1}H-NMR.

$Pb_{0.8}Sn_{0.2}$	Cs	Br	I	FA/GA
feed ratios	0.10	0.15	2.85	0.87/0.03
XPS	0.10 ± 0.013	0.14 ± 0.021	2.86 ± 0.072	−
^{1}H-NMR				0.87/0.029
$Pb_{0.7}Sn_{0.3}$	Cs	Br	I	FA/GA
feed ratios	0.10	0.15	2.85	0.87/0.03
XPS	0.10 ± 0.015	0.15 ± 0.019	2.84 ± 0.069	−
^{1}H-NMR				0.87/0.027
$Pb_{0.6}Sn_{0.4}$	Cs	Br	I	FA/GA
feed ratios	0.10	0.15	2.85	0.87/0.03
XPS	0.10 ± 0.016	0.15 ± 0.027	2.83 ± 0.075	−
^{1}H-NMR				0.87/0.026

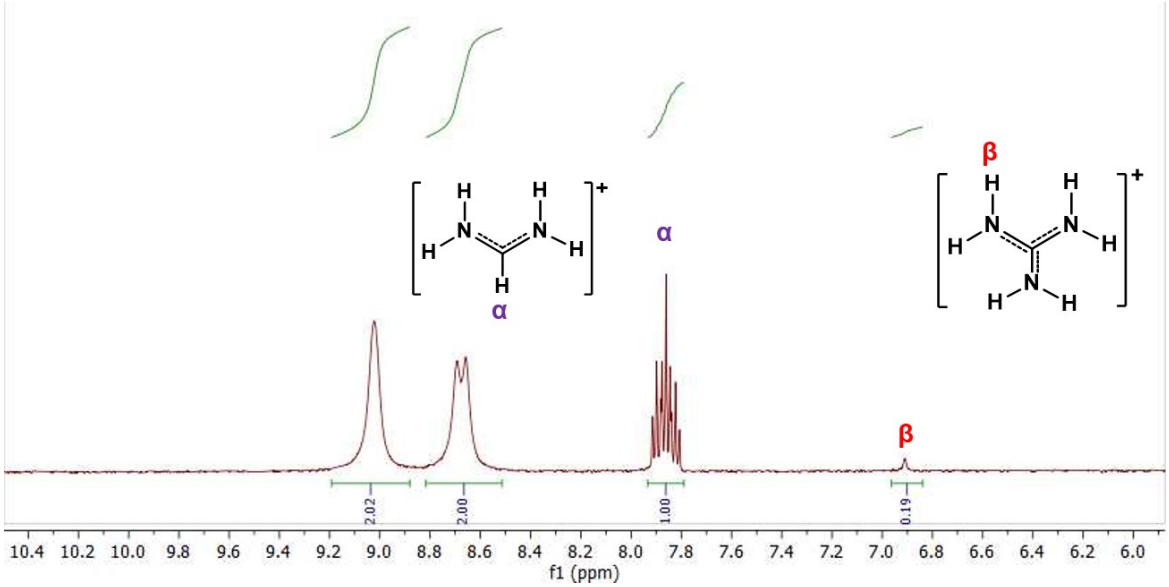

Supplementary Figure 2. NMR characterization of grounded powders obtained from single crystals. ^{1}H-NMR spectra of $Pb_{0.7}Sn_{0.3}$ crystal-dissolved solution in deuterated N,N-dimethylsulfoxide (DMSO) at 295 K. For the Pb:Sn feed ratios of 8:2 and 6:4 in the growth solution, the derived ratios between FA and GA remain fairly static. The chemical shifts of 7.87 ppm and 6.90 ppm correspond to -NH- (FA^{+}) and -NH_2 (GA^{+}) groups, respectively. Thus, the chemical formula between FA and GA could be calculated as 1:0.032, similar to the feed ratio.

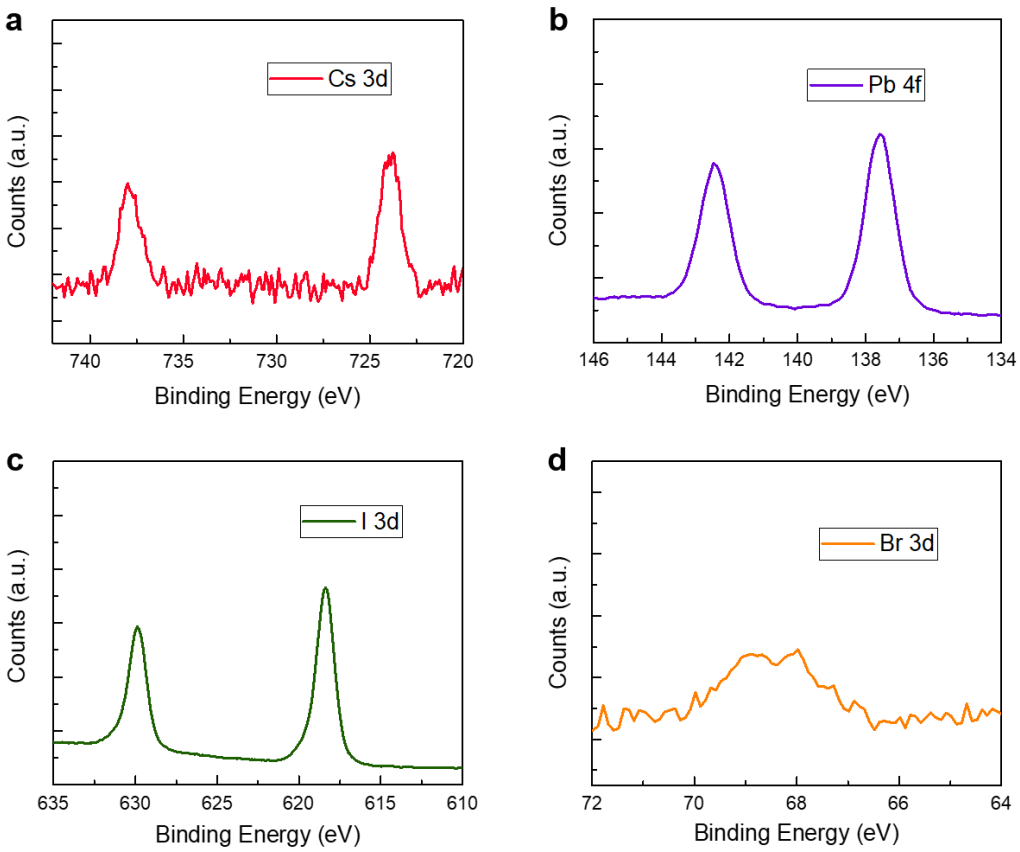

Supplementary Figure 3. XPS profiles of $Pb_{0.7}Sn_{0.3}$ crystal prepared under middle oxygen concentration atmosphere. (**a**) Cs 3*d*, (**b**) Pb 4*f*, (**c**) I 3*d*, and (**d**) Br 3*d*.

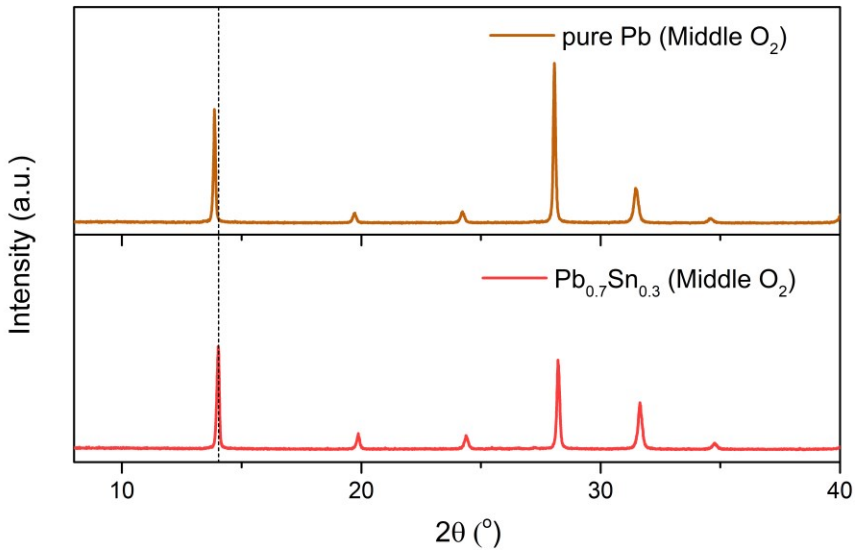

Supplementary Figure 4. XRD patterns of grounded powders obtained from single crystals. We are not able to identify any signal of the impurity phase in all samples prepared by $Cs_{0.1}FA_{0.87}GA_{0.03}Pb(I_{0.95}Br_{0.05})_3$ (pure Pb) and $Pb_{0.7}Sn_{0.3}$ growth solution from powder XRD patterns. We also noticed the shifting of diffraction peaks. It is associated with the smaller ionic radius of tin ions compared to lead ions in the perovskite structure.

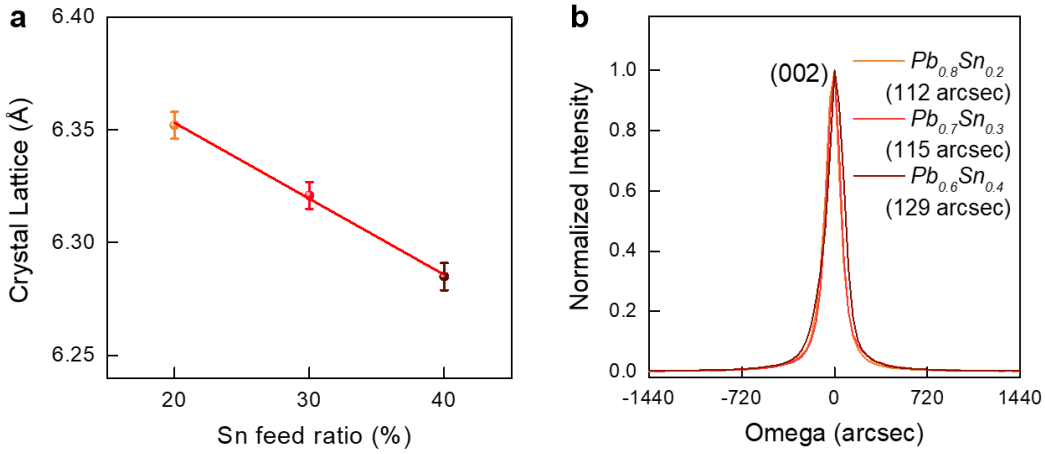

Supplementary Figure 5. Crystal Properties of $Pb_{0.8}Sn_{0.2}$, $Pb_{0.7}Sn_{0.3}$, and $Pb_{0.6}Sn_{0.4}$ single crystals. a, The crystal lattice value derived from the XRD pattern of Figure 1c. The error bars are from experimental uncertainties. **b**, High-resolution XRD rocking curve of the (002) diffraction peak of various single crystals.

Note: The relatively small full-width at half-maximum (FWHM) of the XRD ω-scan indicates the high quality of metal alloyed perovskite single crystals.

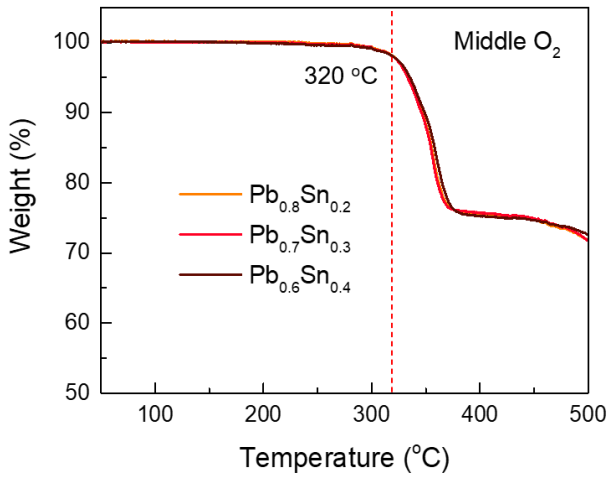

Supplementary Figure 6. Thermogravimetric analysis (TGA) curves of the Pb−Sn alloyed single crystals as a function of the Sn concentration in the growth solution. The curves show that the MA-free Pb−Sn crystals exhibit excellent thermal stability without decomposition until 320 °C, irrelevant to the Sn ratio.

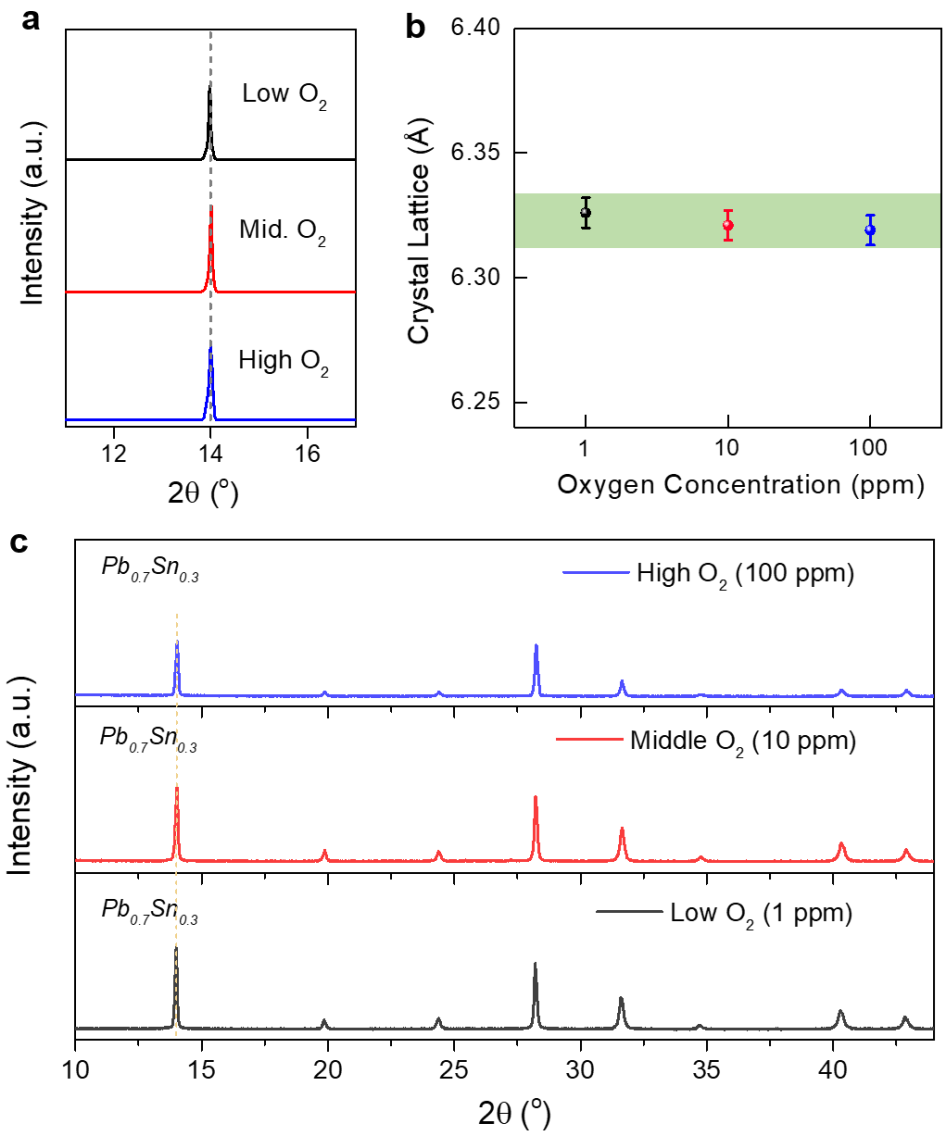

Supplementary Figure 7. Crystal Properties of $Pb_{0.7}Sn_{0.3}$ single crystals prepared by different oxygen concentrations of the surrounding atmosphere. a, Enlarged region of (001) plane of X-ray 2θ scan on the top facet. **b**, The crystal lattice value derived from the X-ray 2θ scan pattern. The error bars are from experimental uncertainties. **c**, XRD patterns of grounded powders obtained from $Pb_{0.7}Sn_{0.3}$ single crystals prepared under different oxygen concentrations of surrounding atmospheres. We are not able to identify any signal of the impurity phase in all samples from powder XRD patterns.

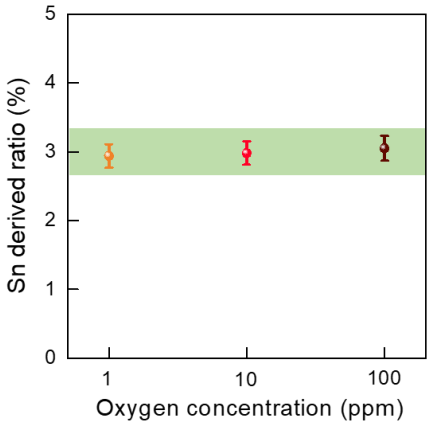

Supplementary Figure 8. Derived [Sn]/([Sn]+[Pb]) atomic ratios from the ICP-OES as a function of the oxygen concentrations of the outside atmosphere. The error bars are from experimental uncertainties.

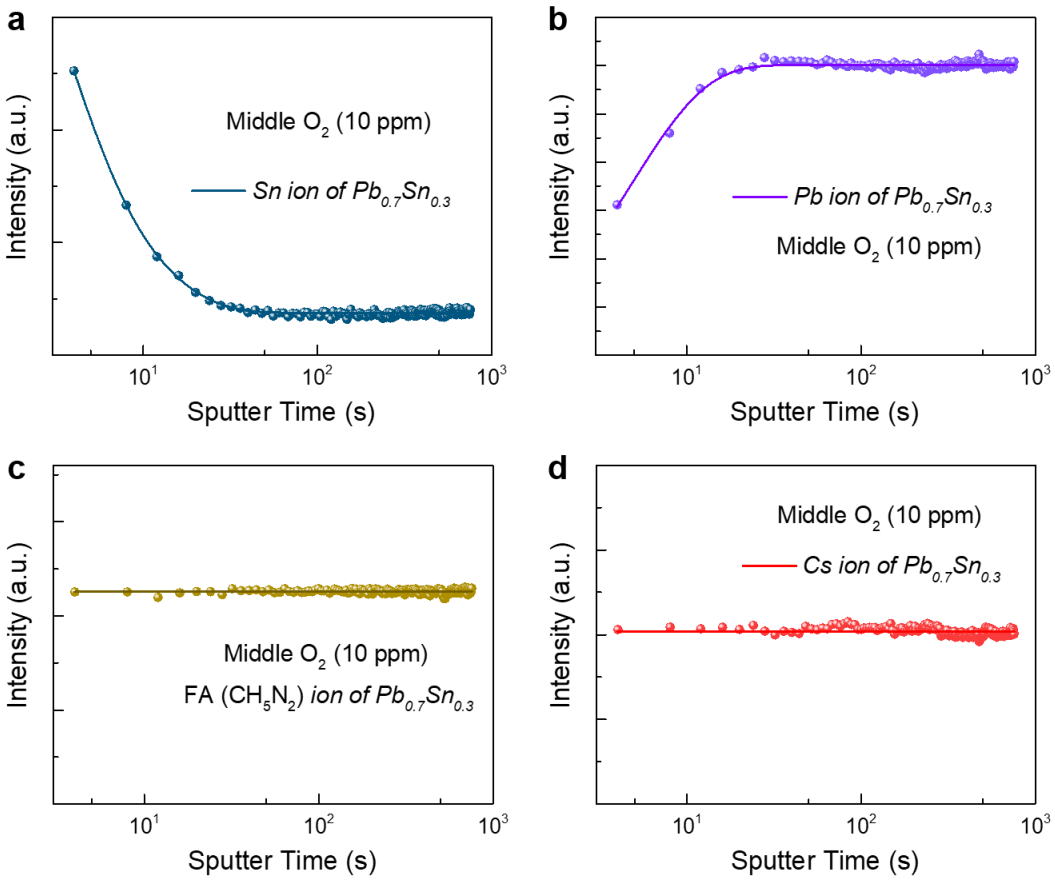

Supplementary Figure 9. Positive mode TOF-SIMS depth profiling of $Pb_{0.7}Sn_{0.3}$ single crystals prepared under middle oxygen concentration atmosphere. Sn (**a**), Pb (**b**), FA (**c**), and Cs (**d**) ions. The sputter rate is set to 8 nm/s.

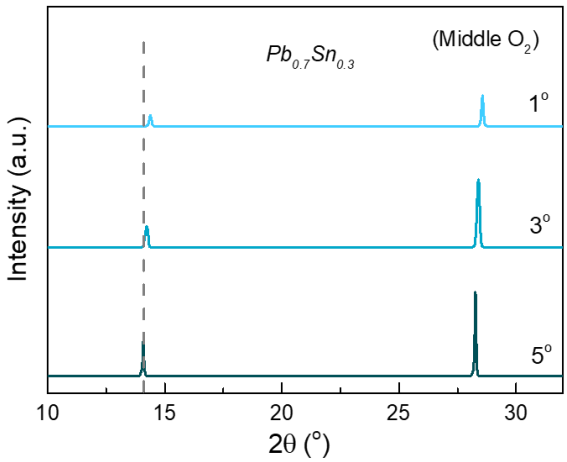

Supplementary Figure 10. GIXRD patterns of $Pb_{0.7}Sn_{0.3}$ single crystals obtained by varying the incident angles from 1° to 5°.

Note: The penetration depth of X-ray into perovskite film at different incident angles, calculated by the formula: $Z = \sin\alpha/\mu$, where α is the incident angle, and μ is the attenuation coefficient. For the incidence angle of $\alpha = 1°$ and $\alpha = 5°$, the X-ray source can penetrate to the top ~200 nm and ~800 nm of the perovskite crystals, respectively.

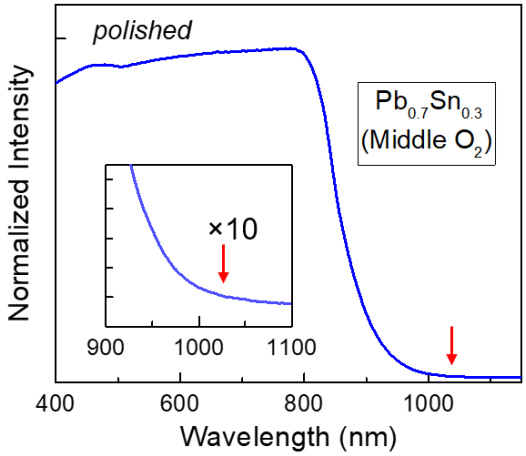

Supplementary Figure 11. Optical absorption spectra of $Pb_{0.7}Sn_{0.3}$ crystals after polishing treatment. The polishing treatment eliminated the absorption features of the Sn-enriched top surface.

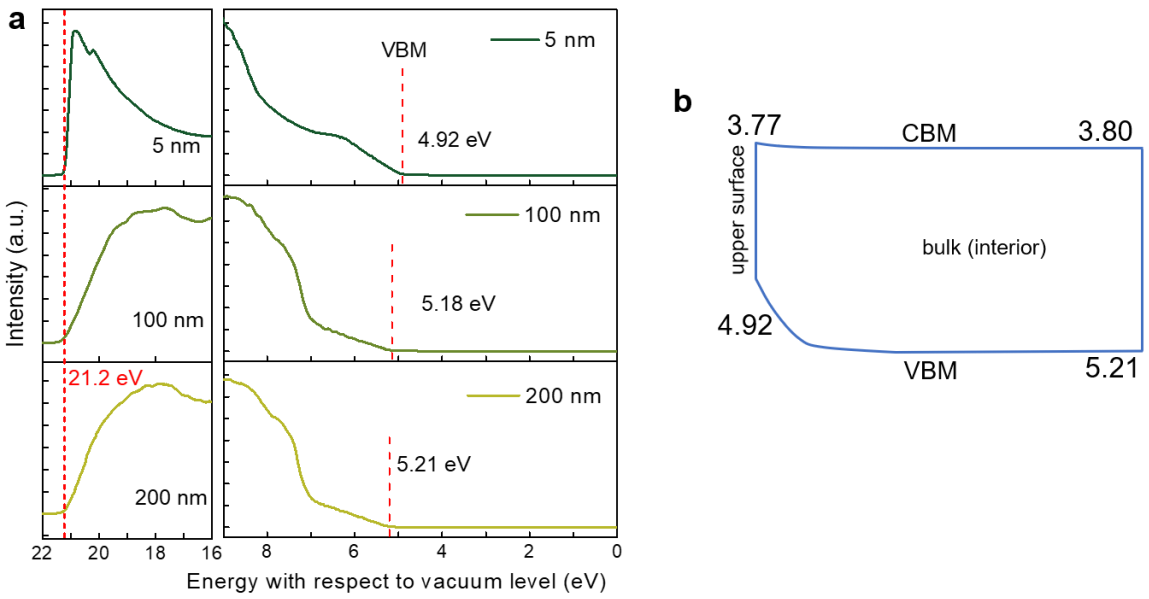

Supplementary Figure 12. Energy level alignment in the vertical direction. a, Depth profiles provided by UPS analysis based on Pb−Sn alloyed perovskite single crystals prepared under the middle oxygen concentration atmosphere. For better comparability, the curves are offset vertically and the high-energy cutoffs are aligned at the excitation energy of 21.2 eV (Left). The extracted positions of VBM are given. **b**, The energy alignment is presented, in which the CBM values are extracted from the EQE bandgap.

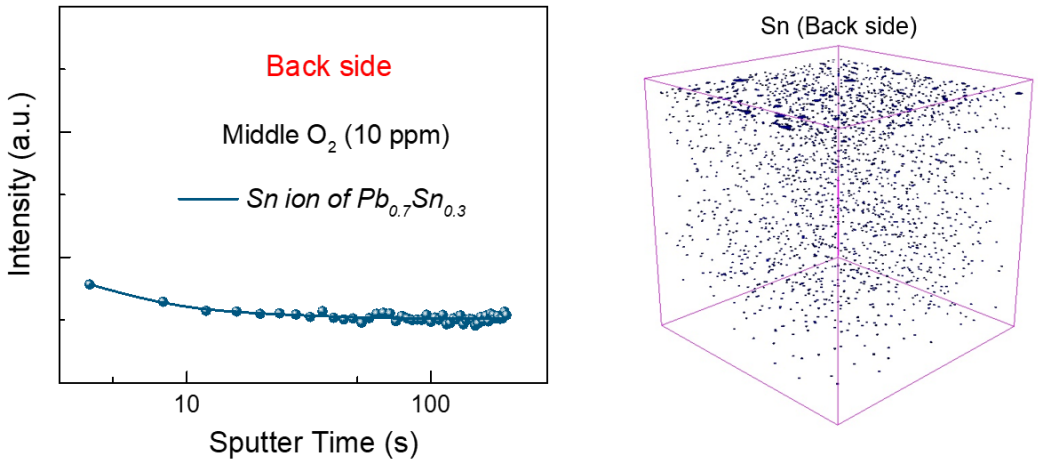

Supplementary Figure 13. TOF-SIMS depth profiling of Sn ions in $Pb_{0.7}Sn_{0.3}$ single crystals prepared under middle oxygen concentration atmosphere, measured from the bottom side to the inner bulk.

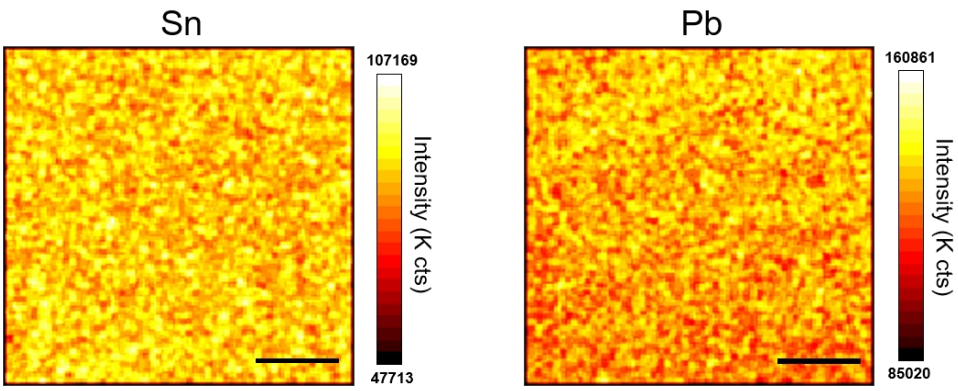

Supplementary Figure 14. AES mapping of Sn and Pb distribution on the top surface of $Pb_{0.7}Sn_{0.3}$ single crystals prepared under middle oxygen concentration atmosphere. Using the characteristics of the Auger spectrum with small spot high spatial resolution images (resolution limit), we found a basically uniform distribution for the metal ions. Scale bar, 5 μm.

Note: AES, reflecting the atomic concentration of each primary element, produces information from the outermost surface of samples (~5 nm), which is more surface sensitive than electron microscopy[8].

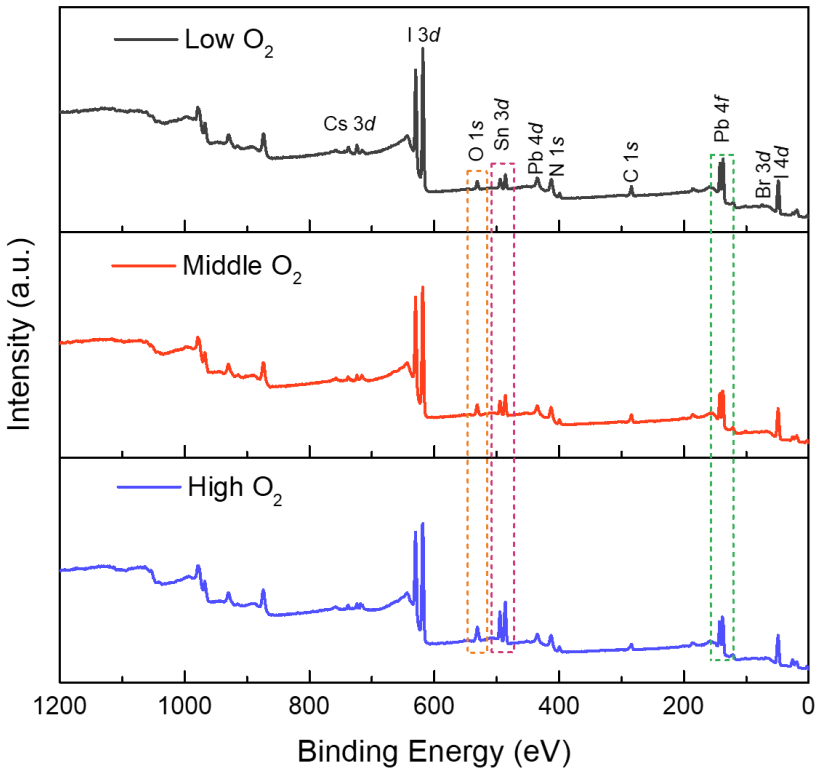

Supplementary Figure S15. The full XPS survey spectra. Survey XPS spectra obtained from the top surface of $Pb_{0.7}Sn_{0.3}$ perovskite crystals prepared under different O_2 concentrations.

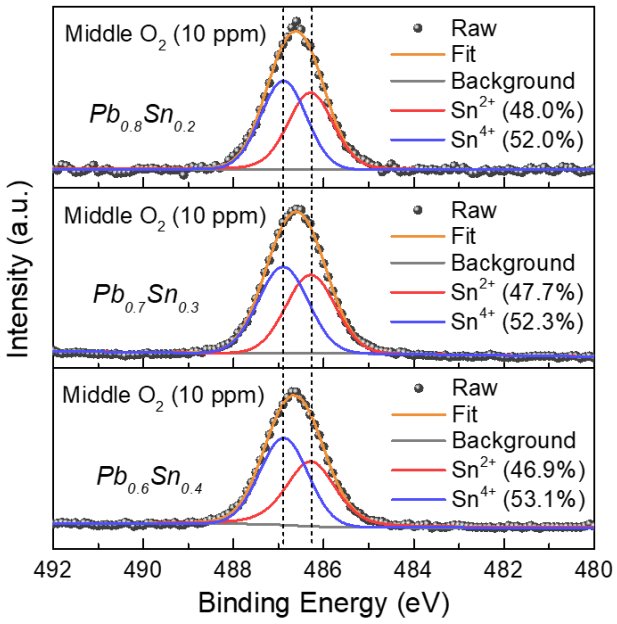

Supplementary Figure S16. XPS of Sn 3*d* core peaks. Performed on the top surface of Pb−Sn alloyed perovskite single crystals with different Pb:Sn feed ratio in the solution.

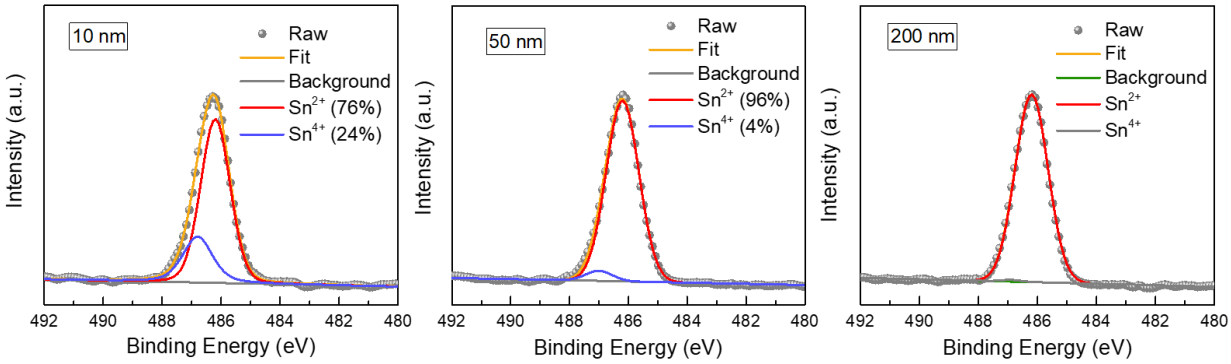

Supplementary Figure S17. XPS depth analysis. XPS analysis of Sn 3*d* peaks in the $Pb_{0.7}Sn_{0.3}$ perovskite crystal with varied argon etching thickness from the top surface.

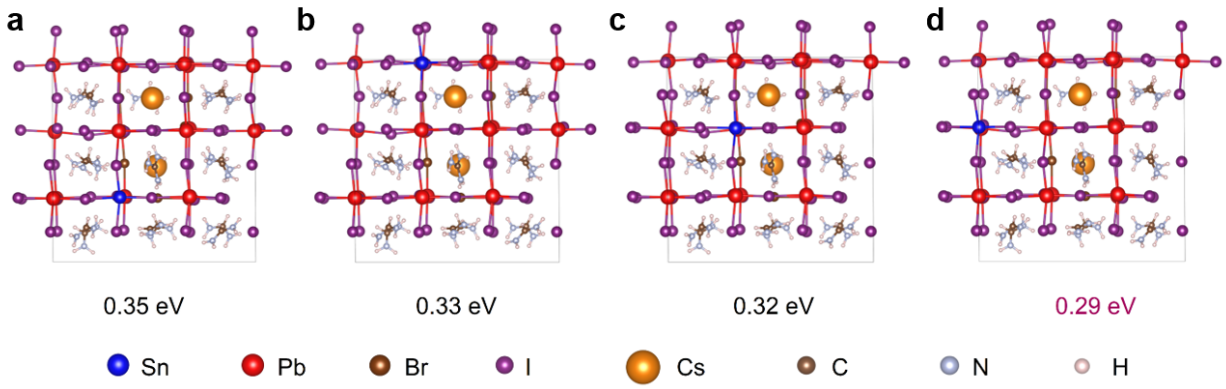

Supplementary Figure 18. DFT-optimized structures. Optimized supercell structures of pure Pb perovskite with one Sn replacing Pb with (**a**) one nearest GA, (**b**) one nearest Cs, (**c**) one nearest GA and one nearest Cs, and (**d**) no nearest GA/Cs. The ΔH_f values for Sn replacing Pb are marked below each structure. The lowest formation energy (corresponding to the most likely site) in each configuration is provided in Supplementary Table 3.

Supplementary Table 3. The formation energy of perovskite compositions with various supercell structures relative to the pure-Pb structure[7].

Abbreviation	Composition	Formation energy relative to pure-Pb (eV)[a]
pure-Pb	$Cs_2FA_{15}GA_1Pb_{18}I_{51}Br_3$	0
Pb−Sn alloying (direct)	$Cs_2FA_{15}GA_1Pb_{17}Sn_1I_{51}Br_3$	0.29
Pb−Sn alloying (O_2-incorporated)[b]	$Cs_2FA_{15}GA_1Pb_{17}Sn_1I_{50}Br_3O_2$	0.07
Pb−Sn alloying (O_2-incorporated)[b]	$Cs_2FA_{15}GA_1Pb_{16}Sn_2I_{49}Br_3O_4$	-0.32

[a]We replaced Pb atoms with Sn atoms randomly and defined the position with the lowest formation energy as the favorable channel.

[b]In the vacancy-mediated channel, oxygen occupies the sites of iodine vacancy before the substitution of lead for tin.

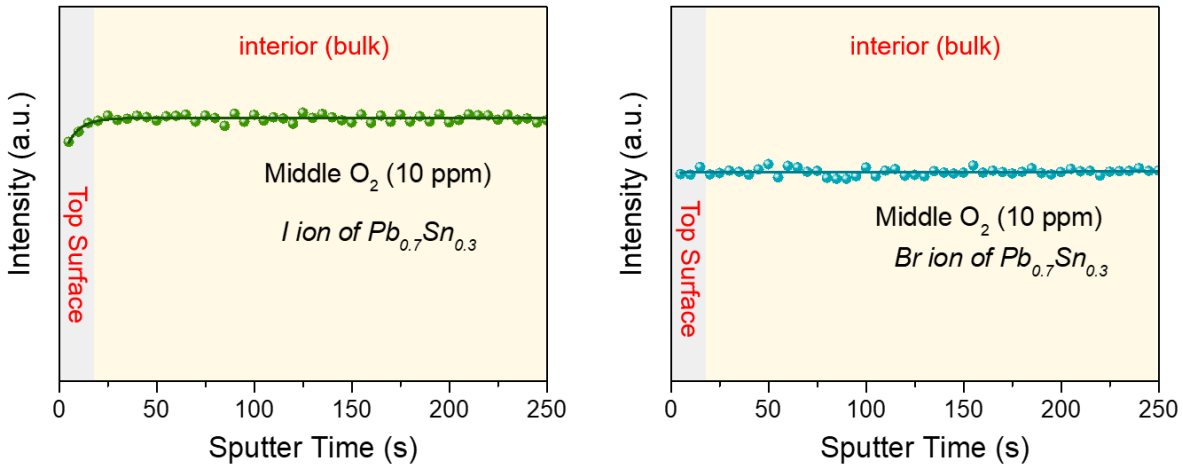

Supplementary Figure 19. Negative mode TOF-SIMS depth profiling. I and Br ions in $Pb_{0.7}Sn_{0.3}$ single crystals prepared under middle oxygen concentration atmosphere from the top surface to the inner bulk. The sputter rate is set to 8 nm s^{-1}.

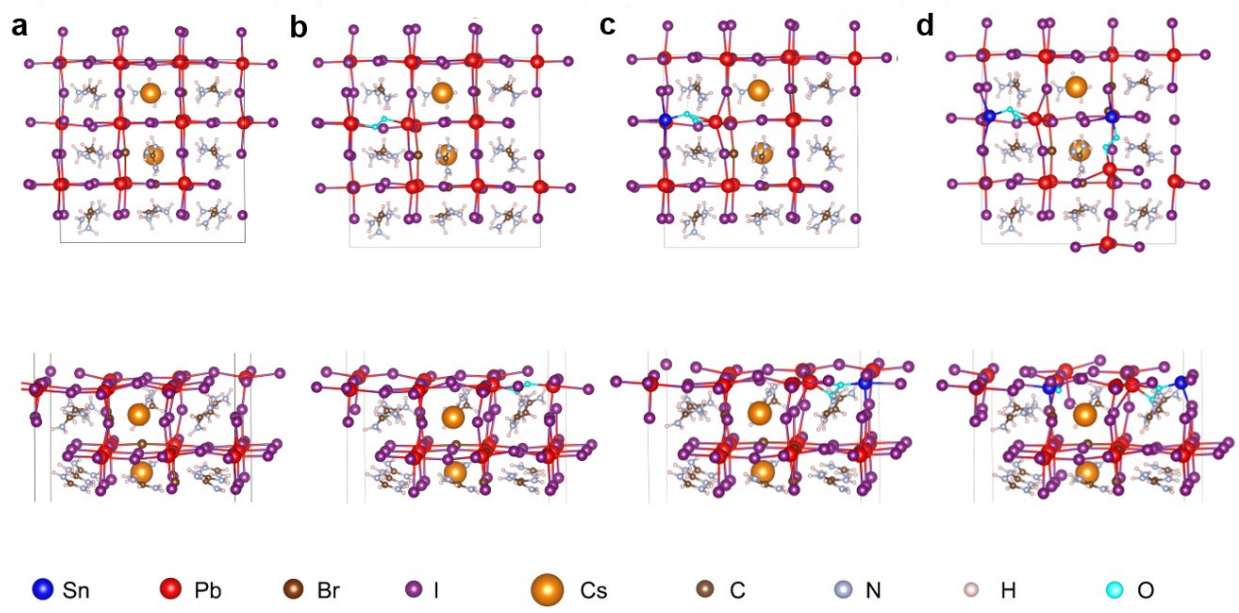

Supplementary Figure 20. DFT-optimized structures with the O_2 incorporation. Top and side view of the optimized supercell structures of (**a**) pure Pb perovskite without modification, (**b**) pure Pb perovskite with one O_2 incorporated into iodide vacancy site, (**c**) Pb-Sn alloying with one Sn ion through the O_2-incorporated channel, and (**d**) Pb-Sn alloying with two Sn ions through the O_2-incorporated channel. We considered different random positions for oxygen incorporation and chose the one with the lowest formation energy (corresponding to the most likely site).

Note: Iodide can be easily oxidized into I_2 and triiodide ions (I_3^- ions) under heating by the oxygen dissolved in solution[9]. To maintain the electrical neutrality, the O_2 molecule takes the place of the I^- anion and forms the superoxide species, O_2^-. DFT results show that oxygen diffusion into the iodine vacancies is favored by 0.21 eV. Thus, iodine vacancy defects act as molecular traps and mediate the electron transfer reaction with oxygen.

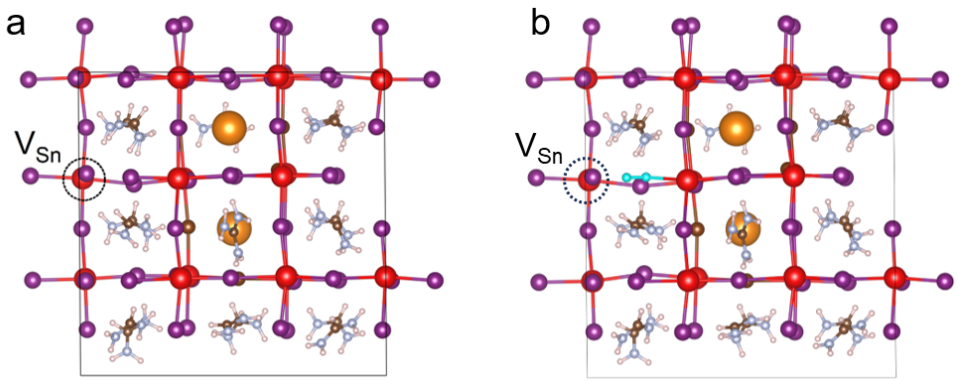

Supplementary Figure 21. Sn vacancy formation energies. (**a**) Pb-Sn alloyed perovskite (direct channel) and (**b**) Pb-Sn alloyed perovskite (O_2-incorporated channel). We considered random positions for Sn vacancies in Pb-Sn alloyed perovskite structures and chose the one with the lowest formation energy (corresponding to the most likely vacancy site).

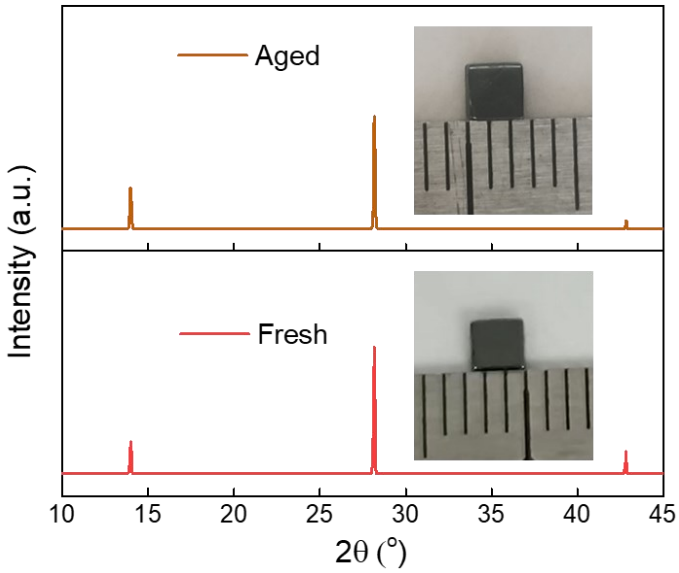

Supplementary Figure 22. Stability evaluation. X-ray 2*θ* scan on the top facet of $Pb_{0.7}Sn_{0.3}$ single crystals prepared under middle oxygen concentrations before and after aging. The insets show the photographs of single crystals before and after exposure in the ambient for six months (25 °C, ~40% RH).

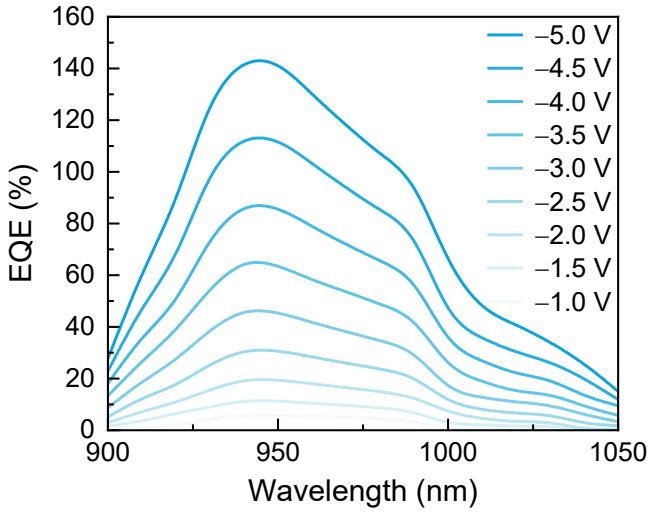

Supplementary Figure 23. The variation of EQE in the infrared band with voltage. EQE slowly increases when the bias increases from −1 V to −2 V. When the bias exceeds −2 V, EQE begins to grow rapidly and exceeds 100% at −4.5 V.

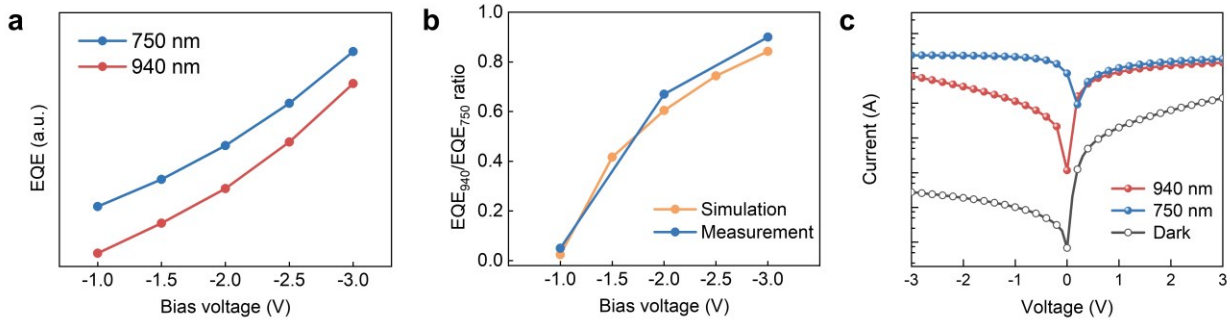

Supplementary Figure 24. COMSOL simulation. a, Simulated EQE results of photodetectors at different wavelengths measured varied bias voltages. **b**, The dependence of the EQE ratio between 750 nm and 940 nm on voltage. **c**, Simulation IV characteristics at dark and under illumination of 750 and 940 nm light.

Note: We selected 750 nm and 940 nm light as the characteristic wavelength to analyze the generation position of short-wavelength and long-wavelength photo-generated carriers, respectively. For the gradient distribution of Sn at the surface, we simplified the process by dividing the 120 nm surface into four regions with different parameters (Supplementary Table 4). In order to approach the actual situation as closely as possible, the optical constants were measured from the perovskite film with the same Pb:Sn ratio of the Sn-rich region derived from the TOF-SIMS results.

Supplementary Table 4. Key parameters used for perovskite photodetector simulation.

Layer[a]	1	2	3	4	5
Perovskite	Sn enriched	Sn enriched	Sn enriched	Sn enriched	bulk
Thickness (nm)	30	30	30	30	5×10^5
μ_h ($cm^2 V^{-1} s^{-1}$)	293	293	293	293	293
μ_e ($cm^2 V^{-1} s^{-1}$)	23.7	23.7	23.7	23.7	23.7
Trap density (cm^{-3})[b]	1×10^{19}	1×10^{17}	1×10^{15}	1×10^{13}	1×10^{12}
k_{750}	0.273	0.259	0.256	0.255	0.255
k_{940}	0.202	0.062	0.028	0.018	0.012

[a]We set up perovskite layers doped with different Sn concentrations based on the measured optical and electrical parameters. Layers 1-4 are surface Sn-rich regions (from the outside to the inside) with a thickness of 30 nm for each layer. Layer 5 is the bulk region with a thickness of 500 μm.
[b]Derived from the results of DLCP measurement.

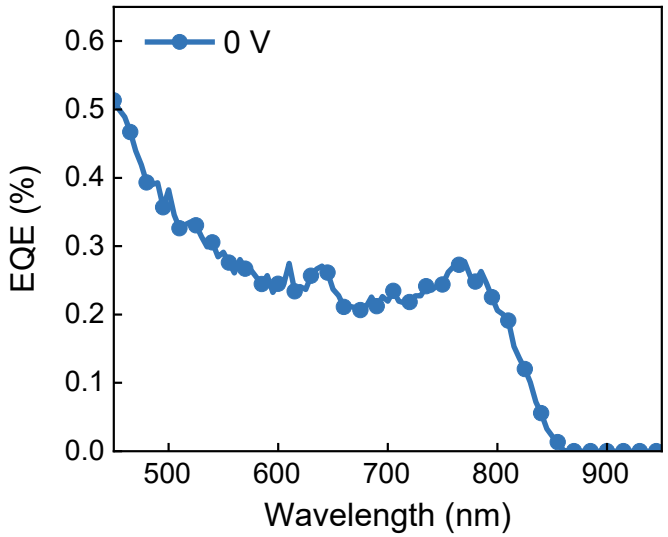

Supplementary Figure 25. EQE results of the perovskite single crystal photodetector measured at 0 V bias. The device can still separate the photo-generated carrier to obtain a photo response without external bias voltage.

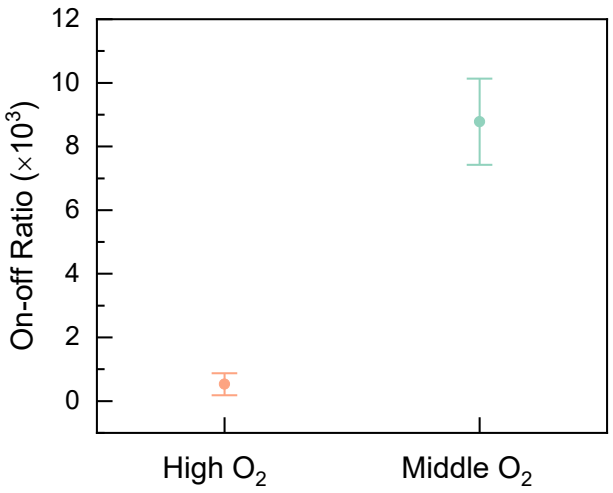

Supplementary Figure 26. The on-off ratio of photodetectors based on $Pb_{0.7}Sn_{0.3}$ perovskite crystals prepared from different oxygen concentration atmospheres. The error bars are from experimental uncertainties.

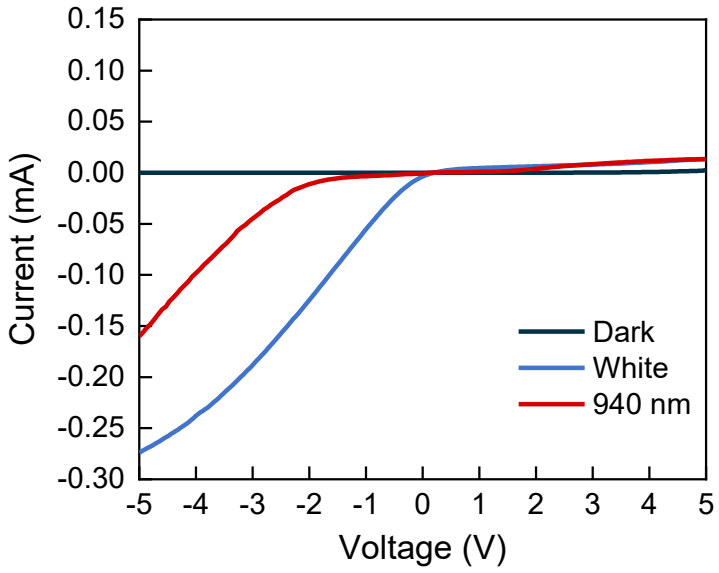

Supplementary Figure 27. The current-voltage curves of the Pb−Sn alloyed single crystal photodetector. Under negative bias, the photocurrent irradiated by white light immediately turns on as the bias increases. In contrast, the photocurrent irradiated by infrared light has a cutoff zone that only turns on when it exceeds −2 V, similar to the characteristics of the infrared region EQE.

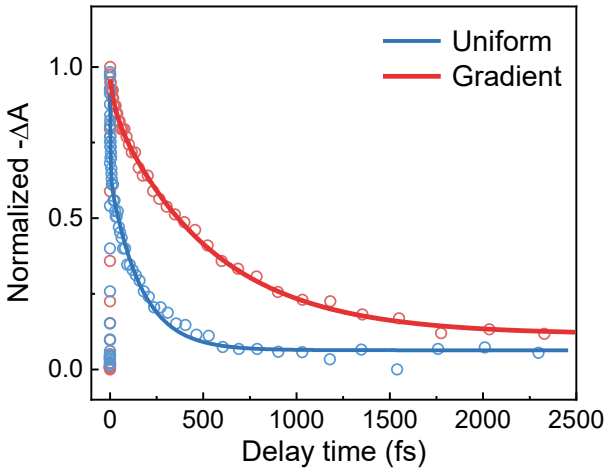

Supplementary Figure 28. TAS kinetic analysis of uniform and gradient Sn distribution samples. The fitting lifetimes of the uniform and gradient distribution samples are 163 and 537 ps, respectively.

Note: To approach the actual situation in the perovskite single crystals, we fabricated two thin-film samples with different Sn distributions (gradient and uniform) by adjusting the process conditions.[10] The increased ground state bleaching signal lifetime indicates that the Sn gradient promotes the separation of photogenerated carriers and suppresses the recombination of non-equilibrium carriers, which is consistent with the illustration in Fig. 3d.

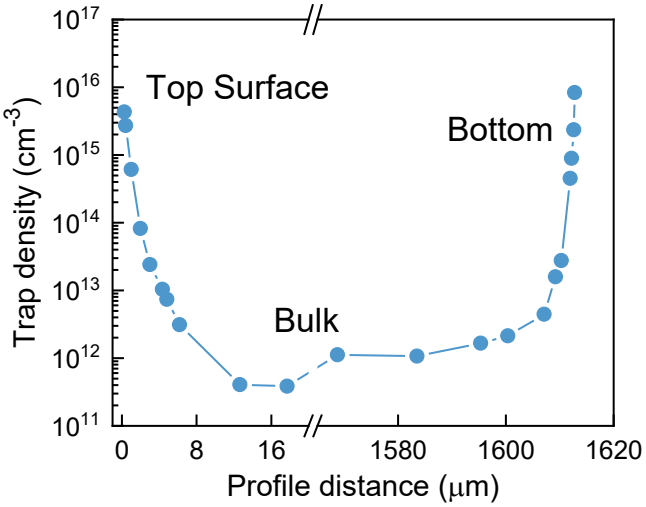

Supplementary Figure 29. DLCP of pure-Pb perovskite single crystals. The trap density of the pure-Pb perovskite single crystal is consistent with the previously reported results[11]. The density of trapped states on the surface is higher than on the body, but the difference between the upper and lower surfaces is insignificant.

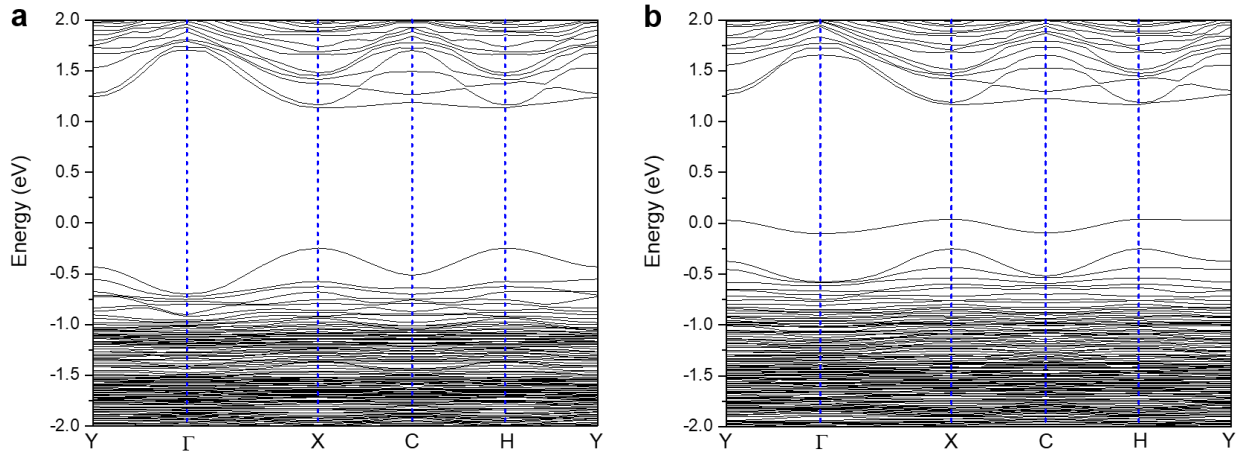

Supplementary Figure 30. Bands structures calculated using GGA-PBE functional. (**a**) Pb−Sn alloyed perovskite (direct channel) and (**b**) Pb−Sn alloyed perovskite (O_2-incorporated channel). The Fermi energy was set at zero.

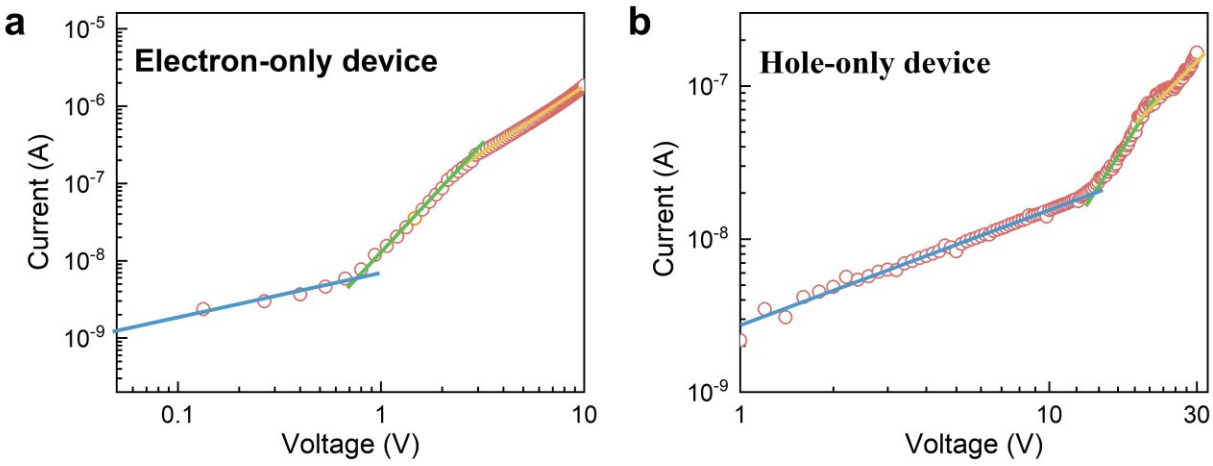

Supplementary Figure 31. The current-voltage curve for single carrier devices of Pb−Sn alloyed single crystal. a, electron-only device. **b**, hole-only device.

Note: The electron-only devices with Cu/C_{60}/Perovskite/C_{60}/Cu structure and hole-only devices with Au/Perovskite/Au structure were prepared for the space charge-limited current method. The curve can be divided into three regions: ohmic region, trap-filling region, and child region. From the transition point of the trap-filling region, we can calculate the trap density (n_t) according to the formula (2)[12]:

$$n_t = \frac{2V_{\mathrm{TFL}}\varepsilon\varepsilon_0}{eL^2} \tag{2}$$

Where V_{TFL} is the trap-filled limit voltage, ε is the relative dielectric constant, ε_0 is the vacuum permittivity, e is the electron charge, and L is the thickness of the single crystal. The hole mobility (μ) could be conservatively determined by Mott-Gurney's SCLC theory from the Child region with the equation (3):

$$J_D = \frac{9\varepsilon\varepsilon_0\mu V_{\mathrm{b}}^2}{8L^3} \tag{3}$$

where V_{b} is applied voltage.

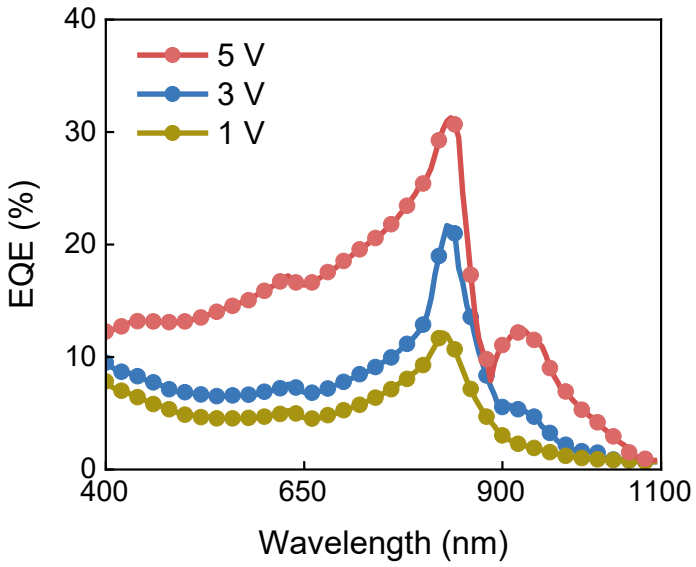

Supplementary Figure 32. The EQE spectra of the perovskite single crystal photodetector measured at different positive biases.

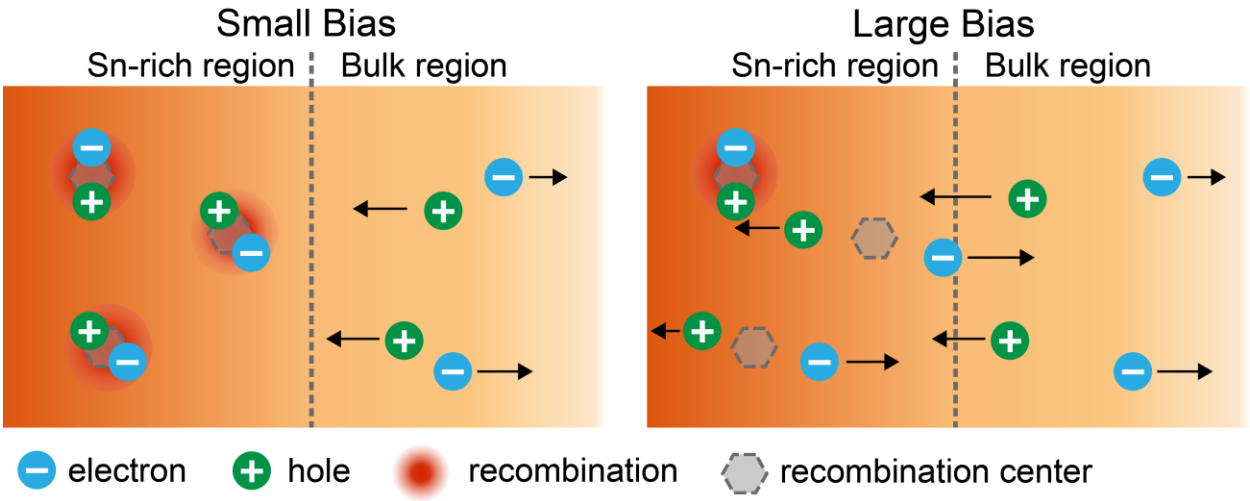

Supplementary Figure 33. Schematic diagrams of the carrier dynamics under different biases in the regions with different recombination center densities. The concentration of recombination centers in different regions affects the overall performance of carrier transport in the device.

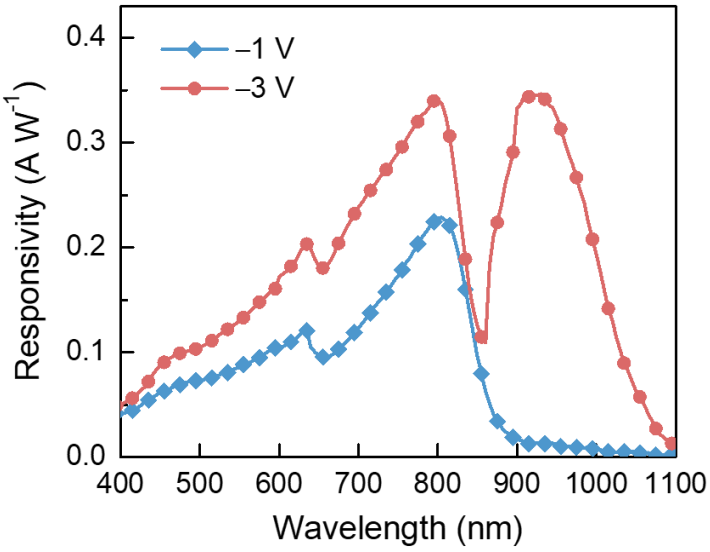

Supplementary Figure 34. The responsivity calculated from external quantum efficiency.

Note: The responsivity can be calculated according to the equation (4):

$$R = EQE \times \frac{q\lambda}{hc} \tag{4}$$

where h is Plank's constant, c is the velocity of light, q is the absolute value of the electron charge, and λ is the light wavelength.

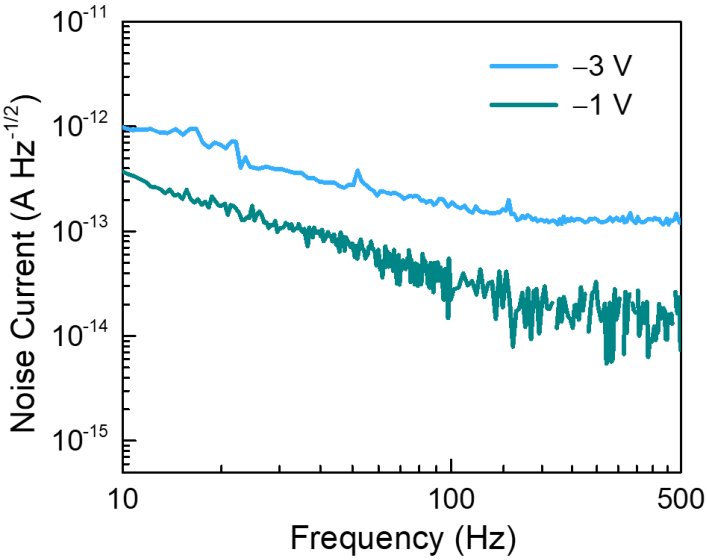

Supplementary Figure 35. The noise current of Pb−Sn alloyed perovskite single-crystal photodetector. The noise current under −3 V is directly measured by the noise analyzer at different frequencies, and the noise current under −1 V is obtained by the Fast Fourier Transform method[13].

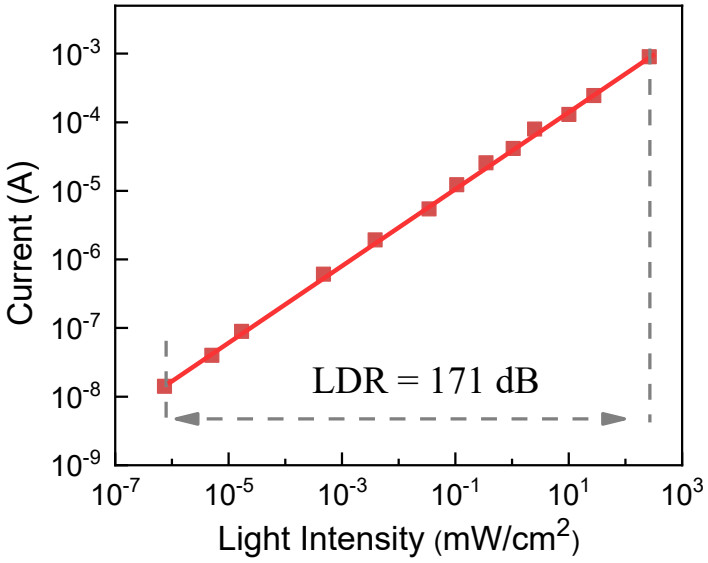

Supplementary Figure 36. LDR of the perovskite photodetector measured at −3 V under 940 nm laser illumination.

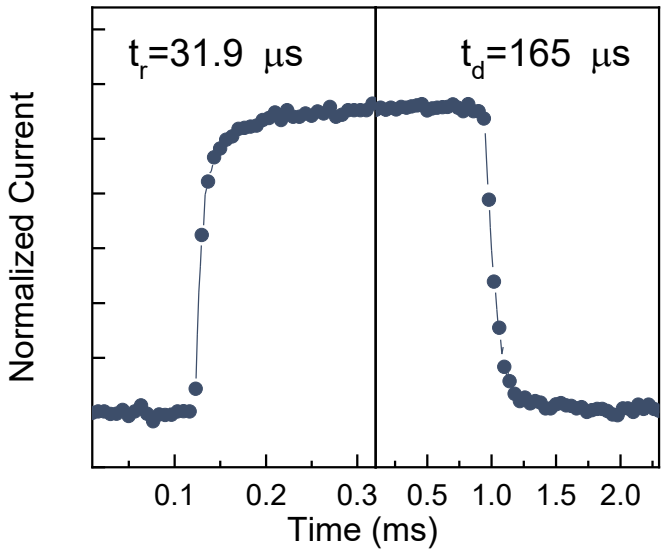

Supplementary Figure 37. The response speed of the photodetector under 940 nm illumination. The rise time of the device is 31.9 μs, and the fall time is 165 μs.

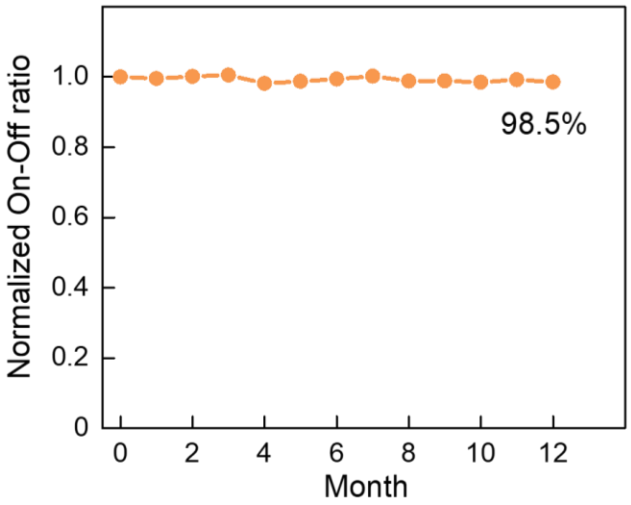

Supplementary Figure 38. Characterization of long-term stability of photodetectors. By recording the on-off ratio under white light irradiation at −1 V bias, the on-off ratio of the device remained at 98.5% of its initial value after 12 months.

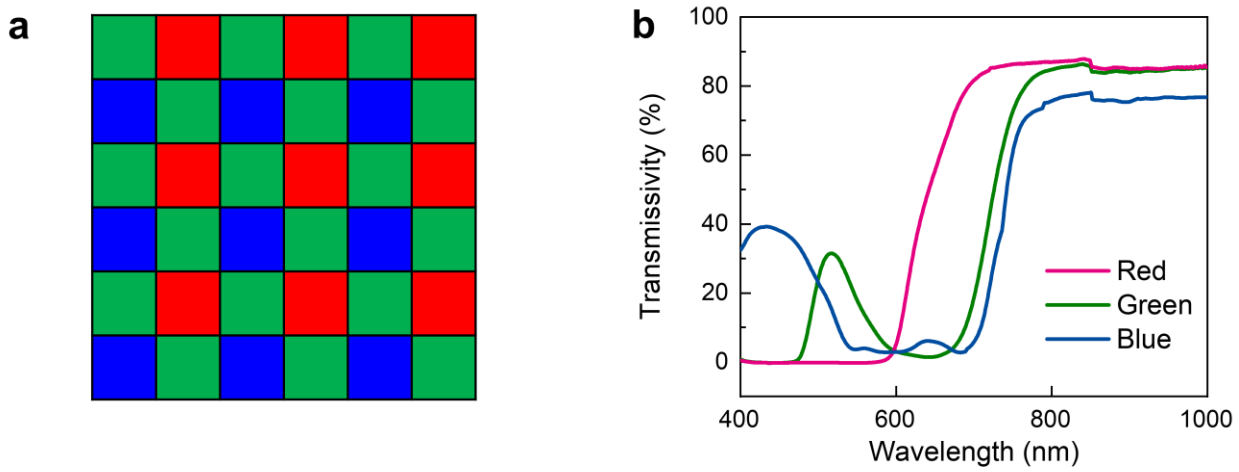

Supplementary Figure 39. Bayer filter characterization. a, Schematic diagram of RGBG type Bayer filter, which is composed of commercial monochrome filters. **b**, The transmission spectra of three monochromatic filters used to produce Bayer filters. It can be seen that three types of filters can distinguish the three primary colors: red, green, and blue, but all transmit infrared light. In addition, the blue filter has a certain transmittance for 532 nm green light, which makes the blue filter area responsive in green light imaging of perovskite and silicon detectors.

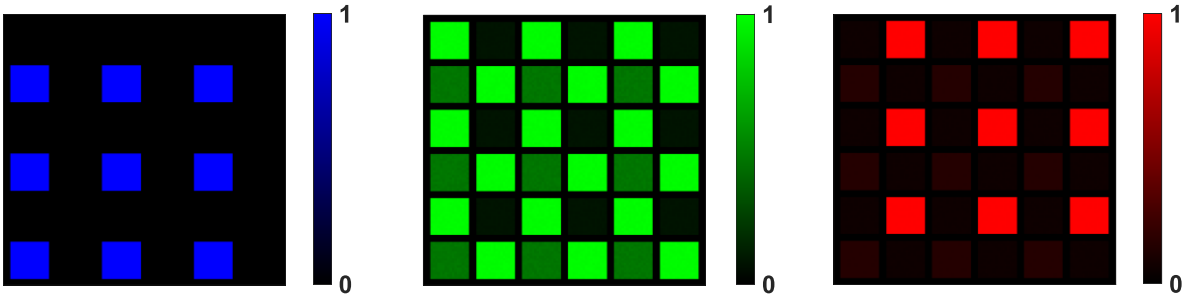

Supplementary Figure 40. Imaging of Bayer filters using a combination of commercial silicon detectors and infrared filters. The imaging results based on the perovskite photodetector are similar to those obtained by stacking a silicon photodetector with an IR-cut filter.

Supplementary Table 5. Color difference (Δ*E*) calculated based on CIEDE2000 issued by the International Commission on Illumination.

Color	$\Delta E_{\text{Perovskite}}$	ΔE_{Si}
Red	0.48	34.65
Green	1.23	6.27
Blue	2.46	34.31

Note: We define the current obtained by photodetectors when Monochromatic light irradiates the corresponding filter as the standard value of the color. Therefore, we map the dark current and photocurrent to [0-255]. Finally, we separated the three colors from the Bayer filter to form the (*R, G, B*) color coordinates under the sRGB standard. Currently, the International Standard CIEDE2000 is considered to be the most perceptually accurate color difference model and is widely used in image quality research. Based on the CIEDE2000 standard, we analyzed the color difference of two photodetectors under infrared interference. We use the imaging results of the silicon detector combined with an infrared filter as the standard monochromatic light. Although the comparison of RGB value is very convenient, using Δ*E* to represent the color distance is more in line with the human eye's ability to distinguish colors. The smaller the value of Δ*E*, the smaller the difference between the compared and standard colors.

According to International Standard *ISO/CIE 11664-6:2014*, the CIEDE2000 color difference formula is as follows (5):

$$\Delta E = \sqrt{\left(\frac{\Delta L'}{k_{\mathrm{L}} S_{\mathrm{L}}}\right)^2 + \left(\frac{\Delta C'}{k_{\mathrm{C}} S_{\mathrm{C}}}\right)^2 + \left(\frac{\Delta H'}{k_{\mathrm{H}} S_{\mathrm{H}}}\right)^2 + R_T \frac{\Delta C'}{k_C S_{\mathrm{C}}} \frac{\Delta H'}{k_{\mathrm{H}} S_{\mathrm{H}}}} \tag{5}$$

where $\Delta L'$ is CIEDE2000 lightness difference, $\Delta C'$ is CIEDE2000 chroma difference, $\Delta H'$ is CIEDE2000 hue difference, S_{L} is lightness weighting function, S_{C} is chroma weighting function and S_{H} is hue weighting function, k_{L}, k_{C} and k_{H} are parametric factors and R_{T} is rotation function.

$$\Delta L' = L_2^* - L_1^* \bar{L} = \frac{L_1^* + L_2^*}{2}, \bar{C} = \frac{C_1^* + C_2^*}{2} \tag{6}$$

where L^* is CIELAB lightness, C^* is CIELAB chroma.

$$a_1' = a_1^* + \frac{a_1^*}{2}\left(1 - \sqrt{\frac{\bar{C}^7}{\bar{C}^7 + 25^7}}\right), a_2' = a_2^* + \frac{a_2^*}{2}\left(1 - \sqrt{\frac{\bar{C}^7}{\bar{C}^7 + 25^7}}\right) \tag{7}$$

where a' and b' are CIEDE2000 a', b' coordinates, a^* and b^* are CIELAB a^*,b^* coordinates.

$$\bar{C}' = \frac{C_1' + C_2'}{2} \; and \; \Delta C' = C_2' - C_1', where \; C_1' = \sqrt{a_1'^2 + b_1^{*2}} \; C_2' = \sqrt{a_2'^2 + b_2^{*2}} \tag{8}$$

where C' is CIEDE2000 chroma, $\bar{C}'$ is arithmetic mean of the CIEDE2000 chromas of two colour stimuli.

$$h_1' = atan2(b_1^*, a_1'), mod\ 360°, h_2' = atan2(b_2^*, a_2'), mod\ 360° \tag{9}$$

where h' is CIEDE2000 hue angle.

$$\Delta h' = \begin{cases} h_2' - h_1' & |h_1' - h_2'| \le 180° \\ h_2' - h_1' + 360° & |h_1' - h_2'| > 180° \quad , h_2' \le h_1' \\ h_2' - h_1' - 360° & |h_1' - h_2'| > 180° \quad , h_2' > h_1' \end{cases} \tag{10}$$

where $\Delta h'$ is CIEDE2000 hue-angle difference.

$$\Delta H' = 2\sqrt{C_1' C_2'} \sin\left(\frac{\Delta h'}{2}\right), \Delta \bar{H}' = \begin{cases} (h_1' + h_2' + 360°)/2 & \left|h_1' - h_2'\right| > 180° \\ \frac{h_1' + h_2'}{2} & \left|h_1' - h_2'\right| \le 180° \end{cases} \tag{11}$$

$$T = 1 - 0.17\cos(\bar{H}' - 30°) + 0.24\cos(2\bar{H}') + 0.32\cos(3\bar{H}' + 6°) - 0.20\cos(4\bar{H}' - 63°) \tag{12}$$

where T is T-function for hue weighting

$$S_L = 1 + \frac{0.015(\bar{L} - 50)^2}{\sqrt{20 + (\bar{L} - 50)^2}}, S_C = 1 + 0.045\bar{C}', S_H = 1 + 0.015\bar{C}'T \tag{13}$$

$$R_T = -2\sqrt{\frac{\bar{C}^7}{\bar{C}^7 + 25^7}} sin\left[60° \cdot exp\left(-\left[\frac{\bar{H}' - 275°}{25°}\right]^2\right)\right] \tag{14}$$

Supplementary References

1. Kresse, G. & Furthmüller, J. Efficient iterative schemes for ab initio total-energy calculations using a plane-wave basis set. *Phys. Rev. B* **54**, 11169 (1996).
2. VandeVondele, J. & Hutter, J. Gaussian basis sets for accurate calculations on molecular systems in gas and condensed phases. *J. Chem. Phys.* **127**, 114105 (2007).
3. Perdew, J. P., Burke, K. & Ernzerhof, M. Generalized gradient approximation made simple. *Phys. Rev. Lett.* **77**, 3865 (1996).
4. Grimme, S. Semiempirical GGA-type density functional constructed with a long-range dispersion correction. *J. Comput. Chem.* **27**, 1787-1799 (2006).
5. Phung, N. et al. The doping mechanism of halide perovskite unveiled by alkaline earth metals. *J. Am. Chem. Soc.* **142**, 2364-2374 (2020).
6. Chen, S., Xiao, X., Gu, H. & Huang J. Iodine reduction for reproducible and high-performance perovskite solar cells and modules. *Sci. Adv.* **7**, eabe8130 (2021).
7. Saidaminov, M. I. et al. Suppression of atomic vacancies via incorporation of isovalent small ions to increase the stability of halide perovskite solar cells in ambient air. *Nat. Energy* **3**, 648-654 (2018).
8. Lin, W. C., Lo, W. C., Li, J. X., Huang, P. C. & Wang M. Y. Auger electron spectroscopy analysis of the thermally induced degradation of $MAPbI_3$ perovskite films. *ACS Omega* **6**, 34606-34614 (2021).
9. Liu, Y. et al. Inch-sized high-quality perovskite single crystals by suppressing phase segregation for light-powered integrated circuits. *Sci. Adv.* **7**, eabc8844 (2021).
10. Cao, J. et al. High-performance tin-lead mixed-perovskite solar cells with vertical compositional gradient. *Adv. Mater.* **34**, 2107729 (2022).
11. Ni, Z. et al. Resolving spatial and energetic distributions of trap states in metal halide perovskite solar cells. *Science* **367**, 1352–1358 (2020).
12. Jiang, J. et al. Synergistic strain engineering of perovskite single crystals for highly stable and sensitive X-ray detectors with low-bias imaging and monitoring. *Nat. Photon*. **16**, 575–581 (2022).
13. Fang, Y. et al. Accurate characterization of next-generation thin-film photodetectors. *Nature Photon.* **13**, 1–4 (2019).